



Earth as an Exoplanet: Investigating the Effects of Cloud Variability on the Direct-imaging of Atmospheres

Soumil Kelkar^{1,2,3} , Prabal Saxena², Ravi Kopparapu² , and Joy Monteiro⁴

¹ Indian Institute of Science Education and Research Pune, Dr Homi Bhabha Road, Pashan, Pune, Maharashtra—411008, India

² NASA Goddard Space Flight Center, 8800 Greenbelt Road, Greenbelt, MD 20771, USA

³ Center for Research and Exploration in Space Science and Technology, NASA/GSFC, Greenbelt, MD 20771, USA

⁴ Departments of Earth and Climate Science and Data Science, Indian Institute of Science Education and Research Pune, Dr Homi Bhabha Road, Pashan, Pune, Maharashtra—411008, India

Received 2024 October 9; revised 2025 February 12; accepted 2025 March 4; published 2025 April 11

Abstract

A planet's spectrum is dynamic and only represents a time-dependent snapshot of its properties. Changing atmospheric conditions due to climate and weather patterns, particularly variation in cloud cover, can significantly affect the spectrum in ways that complicate the understanding of a planet's baseline atmospheric properties. Variable cloud cover and cloud properties affect the detectability of atmospheric constituents, and also greatly influence the radiative transfer that determines a planet's spectrum. This has considerable implications for direct-imaging observations of potentially habitable exoplanets, and thus, it is critical to study and characterize the effects of clouds on their spectra. Clouds have been extensively modeled before, and their effects have been incorporated across climate frameworks spanning a spectrum of complexity. Given the challenges associated with modeling clouds, we adopt a novel approach in this work to study the effects of clouds by using real-time cloud data from Earth observations. Treating Earth as an exoplanet and using detailed observations from the MERRA-2 data collection, we quantify the effects of cloud variability on the spectrum as well as on the detectability of atmospheric constituents, specifically biomarkers like O₂, O₃, and H₂O. The coverage and vertical position of clouds significantly affect the signal-to-noise ratios of these gases and subsequently their detectability in exo-Earth atmospheres. Moreover, we show that variations in the amount of cloud cover will potentially confound efforts to retrieve a stable baseline atmosphere for a planet. This work has important applications to future direct-imaging missions like the Habitable Worlds Observatory.

Unified Astronomy Thesaurus concepts: Atmospheric clouds (2180); Exoplanet atmospheres (487); Direct imaging (387); Biosignatures (2018)

1. Introduction

Among all the 5700 exoplanets detected so far,⁵ there is a significant dearth of exoplanets with properties similar to the inner rocky worlds of our solar system, including Earth (see Figure 1 in B. S. Gaudi et al. 2021). This deficiency is mainly in part due to the higher sensitivity of current detection methods toward massive planets on short orbital periods. To address this issue, the “Pathways to Discovery in Astronomy & Astrophysics for the 2020s” report (National Academies of Sciences, Engineering, and Medicine 2023) recommended an ultraviolet (UV)/optical/infrared space observatory to find and characterize Earth-like planets around nearby stars, specifically the ones that might be potentially habitable. Based on this recommendation, NASA is laying the groundwork for its next flagship mission, currently referred to as the Habitable Worlds Observatory (HWO), which draws from previous mission concepts like the LUVOIR (LUVOIR Team 2019) and Habex (B. S. Gaudi et al. 2020). A significant part of the science precursor work for these mission concepts is devoted to simulating reflected light spectra of planets, computing exposure times, and quantifying the detectability of important

atmospheric constituents and biosignatures. However, the surface of the planet and/or its atmospheric composition may not be homogeneous, and thus, a planet's spectrum is not static but rather dynamic. Moreover, a natural variation in cloud coverage due to weather and climate patterns can also significantly affect the characterization of exoplanet atmospheres.

Clouds are ubiquitous on Earth and other solar system planets, and observations strongly suggest their presence on exoplanets as well (M. R. Line et al. 2013; D. K. Sing et al. 2015; L. Kreidberg et al. 2014). A cloud is defined as the condensate that forms when the vapor pressure of an atmospheric constituent exceeds its saturation vapor pressure (M. S. Marley et al. 2013). In this way, cloud formation provides a sink for an atmospheric constituent. Earth is dominated by clouds composed mostly of water vapor; however, there is a huge diversity in the composition of clouds on planets in our solar system. This includes sulfuric acid clouds on Venus (J. E. Hansen & J. Hovenier 1974), CO₂ ice clouds on Mars (F. Montmessin et al. 2007), and ammonia clouds on Jupiter (T. Brooke et al. 1998), to name a few. Given the diversity in the estimated planetary and atmospheric compositions of exoplanets detected so far, we would also expect their atmospheres to host clouds and other aerosols of varied compositions. A haze is referred to as any condensate produced by photochemistry or other nonequilibrium chemical processes (M. S. Marley et al. 2013); however, the term is often used interchangeably with cloud. A general framework of

⁵ <https://exoplanetarchive.ipac.caltech.edu/>



clouds in the atmospheres of solar system planets is given in A. Sánchez-Lavega et al. (2004), and a comprehensive summary of clouds and cloud formation in exoplanet atmospheres is given in M. S. Marley et al. (2013), C. Helling (2019), and P. Gao et al. (2021).

Clouds affect a planet's radiation budget in three important ways—(i) by reflecting/scattering shortwave stellar radiation back to space, (ii) by absorbing and reemitting longwave thermal radiation emitted by the surface, and (iii) also by emitting their own thermal radiation. Clouds can complicate the radiative transfer processes in an exoplanet's atmosphere and significantly impact the planet's spectrum. Clouds tend to have high albedos, especially in the visible wavelength band, and thus, any planet with a cloudy atmosphere will reflect much more light than a cloudless planet, enhancing the continuum in the reflected light spectrum. Clouds improve the detectability of atmospheric constituents in the visible band, especially those present in significant amounts above the cloud layer, by increasing the albedo and subsequently boosting their absorption signals (Y. Kawashima & S. Rugheimer 2019; J. Wang et al. 2017; Section 3.2 of this work). The effects of clouds on the reflected light spectra were modeled by M. S. Marley et al. (1999), D. Sudarsky et al. (2003), and K. L. Cahoy et al. (2010) for giant exoplanets and by D. Kitzmann et al. (2011a) for Earth-like exoplanets. Since clouds enhance a planet's albedo, they may impact whether a planet is visible or not via direct-imaging. The impact of clouds on the planet's albedo is explored in D. Kitzmann et al. (2011b). Clouds are a significant contributor to the greenhouse effect as they absorb and reemit outgoing longwave radiation emitted by the surface. Thus, the presence of clouds has a profound impact on the thermal emission spectrum of a planet. Due to the greenhouse effect, clouds dampen the spectral features of certain gases in the infrared. The effects of clouds on the thermal emission spectra of planets have been discussed in G. Tinetti et al. (2006), T. Hearty et al. (2009), D. Kitzmann et al. (2011b), and M. Vasquez et al. (2013). Furthermore, clouds also affect spectral signatures originating from the surface, for example, the vegetation red edge signal characteristic of surface vegetation, as shown in models (G. Tinetti et al. 2006; P. Montanes-Rodriguez et al. 2006) and observations of Earth (L. Arnold et al. 2002; S. Hamdani et al. 2006).

Clouds have been extensively modeled with different models spanning a spectrum of complexity. The simplest of cloud models are parameterized models (P. Gao et al. 2021 and references therein), which are typically used for retrieval studies. These models do not include any treatment of the physical processes associated with cloud formation and composition but simply use a set of parameters to estimate the first order effects of clouds. More complex models, on the other hand, involve cloud microphysics, and they typically assume a functional form for the cloud particle size distribution. These cloud models are incorporated into general climate model frameworks ranging from 1D radiative-convective models to 3D general circulation models (GCMs). 1D climate models, by virtue of their definition, cannot estimate differences in horizontal cloud coverage and thus cannot model atmospheres with patchy clouds. Naturally, they also neglect significant multidimensional circulation phenomena, which impact cloud properties. 3D GCMs can accurately model the spatial extent of clouds on a planetary scale; however, they can sometimes be too computationally expensive to run, especially

if complex cloud microphysical processes are involved. Uncertainties in quantifying cloud feedbacks and difficulties in resolving clouds on large model grids (V. Kofman et al. 2024) signify that there are still challenges involved in the accurate representation of clouds in 3D GCMs. There are additional challenges to modeling clouds on terrestrial exoplanets due to a lack of observational constraints on the type and composition of their atmospheres. Uncertainties in observed atmospheric compositions and theoretical predictions make it difficult to accurately estimate the composition and spatial extent of clouds. Nevertheless, clouds have been modeled on terrestrial exoplanets using a variety of approaches. The simplest models modify the surface albedo of the planet to mimic the effects of clouds (J. F. Kasting et al. 1993; A. Segura et al. 2003, 2005; J. L. Grenfell et al. 2007). In this approach, there are no physical assumptions made about the properties of clouds, and it does not impact radiation in the same way as real clouds; hence, these models cannot be used to study the impact of clouds on exoplanet spectra. In more complex models, the properties of clouds and the atmosphere itself are assumed or are constrained to some extent via observations. This approach has been used to model clouds on Earth-like exoplanets using Earth as a reference (L. Kaltenegger et al. 2007; D. Kitzmann et al. 2010). For a more comprehensive description of the intricacies of cloud modeling and the different types of cloud models present in literature, refer to M. S. Marley et al. (2013) and P. Gao et al. (2021).

Given the challenges associated with modeling clouds, one strategy for an accurate examination of the impact of clouds and cloud variability on terrestrial Earth-like planets involves using real-time cloud data from Earth observations. Several Earth-observing satellites collect real-time data crucial for climate monitoring and weather forecasting. These data are assimilated into data products, which can be extracted to obtain atmospheric constraints and real-time values of atmospheric temperature, mixing ratios of gases, and, more importantly for this study, cloud properties. Earth's patchy cloud cover is unique among its terrestrial neighbors. Real-time data from satellites can be leveraged to study the temporal and spatial extent, composition, and albedo of clouds. Data gathered over different portions of the globe can be integrated to produce full-disk observations and global maps of cloud cover. Such integrated disk observations are essential to quantify the impact of clouds on the planetary spectrum, as future direct-imaging missions will only have a full integrated disk view of exoplanets. Moreover, such globally integrated data can be utilized to assess the impact of cloud variability across different temporal and spatial scales on planetary spectra. Real-time data have been extensively used to study cloud properties and quantify trends in cloud coverage over different scales (W. B. Rossow & A. A. Lacis 1990; L. Stowe et al. 1991; D. Wylie et al. 2005; D. Wu et al. 2011; M. D. King et al. 2013). Earth's cloud cover shows significant variation across different spatial and temporal scales. Clouds are nonuniformly distributed across different latitudes. The cloud cover over oceans is significantly higher than land cloud cover. Cloud cover variations over diurnal and seasonal scales are also well documented (M. D. King et al. 2013). Such significant cloud variability influences full-disk observations and subsequently impacts the planet's spectrum.

The studies described above that have modeled the effects of clouds on reflection and emission spectra, planetary albedo

have relied on parameterized cloud models. In this work, we adopt a novel approach, which involves using real-time empirical cloud data from Earth observations to study cloud effects. This allows us to incorporate realistic cloud distributions, which are more accurate than the distributions simulated by cloud models, as well as analyze the effects of naturally varying cloud cover. Our results computed using empirical 3D cloud distributions complement previous results obtained using cloud models. For example, D. Kitzmann et al. (2011b) and Y. Kawashima & S. Rugheimer (2019) use a 1D climate model coupled with a parametric cloud model to quantify the effects of different amounts of low-level and high-level cloud cover on the reflection spectra, and we complement their results (in Section 3.3).

In the context of the future direct-imaging missions whose main goal is to find and characterize nearby Earth-like exoplanets, an investigation into the impacts of clouds on the characterization of exo-Earth atmospheres stands as an important science precursor. In this study, we treat Earth as an exoplanet, and utilize real-time data from the Modern-Era Retrospective analysis for Research and Applications, Version 2 (MERRA-2; R. Gelaro et al. 2017) data set to conduct a detailed analysis of the effects of cloud variability on its spectrum. We also conduct a comparison between all the future direct-imaging mission concepts and evaluate their performance in characterizing different exo-Earth atmospheres with varying cloud cover.

2. Methods

In this study, we use real-time remote sensing Earth data to construct an accurate 3D model of an Earth twin or an exo-Earth. MERRA-2 (R. Gelaro et al. 2017) is a NASA atmospheric reanalysis produced with the Goddard Earth Observing System, Version 5 data assimilation system. Reanalysis is a process where an already existing data assimilation system is used to reprocess meteorological observations. MERRA-2's continuous data record spans from 1980 to the present and contains either instantaneous or time-averaged data products. MERRA-2 relies on an underlying forecast model to combine raw data from disparate observations in a physically consistent manner, enabling the production of gridded data sets for a broad range of variables (R. Gelaro et al. 2017). MERRA-2 has several data collections, each corresponding to different temporal resolutions, surface and atmospheric parameters, aerosol properties, etc. Specifically, we use the M2I3NVASM data collection (Global Modeling and Assimilation Office (GMAO) 2015a), which is an instantaneous 3D gridded data collection that consists of assimilations of meteorological parameters. Each data file is a snapshot of atmospheric properties, captured every 3 hr. We extract all the relevant atmospheric parameters such as temperature, wind speeds, and mixing ratios of ozone, water vapor, liquid water, and water-ice clouds (constituents, which are not well mixed in the atmosphere). The data have a temporal resolution of 3 hr and a horizontal spatial resolution of 0.5° latitude \times 0.625° longitude. The atmosphere is divided into 72 model levels from the surface to 0.01 hPa. Thus, this data collection allows us to examine cloud variability at different temporal scales and subsequently construct a dynamic 3D exo-Earth model with cloudy patches, which exhibit significant variations over time. Spatial variations over latitudinal scales are averaged over since we are considering a planet at

quadrature orbiting in an edge-on orbit. These variations would be much more relevant when considering planets with a nonnegligible system inclination relative to the observer (e.g., oriented in a face-on or a near face-on configuration). Hence, when considering the impacts of cloud variability, we are only concerned with temporal variations in a globally averaged cloud cover.

To construct the ground map, we use data from the MODerate resolution Imaging Spectroradiometer (MODIS; M. Friedl & D. Sulla-Menashe 2015) instrument on board the Terra and Aqua satellites, which takes high-resolution maps of the Earth's surface. This allows us to accurately replicate Earth's ocean and landmass distributions in our exo-Earth model. MODIS data have a resolution of 0.05° latitude \times 0.05° longitude. We assume that the surface is static, in order to eliminate any changes on the surface (for, e.g., change in albedo due to varying snow cover or seasons) from impacting the spectra. In this way, we can attribute any change in spectra to be caused by variations in atmospheric conditions, specifically cloud variability.

Given our exo-Earth model, we use the Planetary Spectrum Generator (PSG; G. L. Villanueva et al. 2018) to simulate observations of this planet. PSG is a radiative transfer model suite that combines state-of-the-art radiative transfer codes, spectroscopic and planetary databases to accurately synthesize and retrieve planetary spectra for any given planetary system. It can simulate observations for a broad range of wavelengths from any given observatory or mission concept. We specifically use the Global Emission Spectra (GlobES) module of PSG, which ingests our 3D exo-Earth model and accurately simulates the spectrum given a range of observational and instrumental parameters. The different aspects of the calculations done will be explained here briefly, but to find out more about using PSG, please refer to the web interface,⁶ the original paper describing the tool (G. L. Villanueva et al. 2018), a recent paper describing the use of PSG to simulate directly imaged exoplanet spectra (P. Saxena et al. 2021), or the PSG documentation handbook (G. L. Villanueva et al. 2022).

GlobES can ingest GCM files, which are converted from the typical netCDF data format. Based on the python codes supplied on the PSG Github page,⁷ we develop an efficient pipeline that retrieves data from the MERRA-2 online data repository,⁸ constructs an accurate 3D model of an exo-Earth from this empirical data, converts the model into a GCM file, which can be uploaded to GlobES, and finally retrieves the simulated spectrum. In addition to atmospheric data, the GCM file also includes information about the orbital configuration of the planet, the geometry of the planetary system with respect to the observer, the specific details of the instrument used to observe the system, and a noise model that incorporates different sources of noise. The entire list of parameters that can be specified in the GCM file can be found on the PSG web interface.⁹

We assume a simplified fiducial exo-Earth that is situated 10 pc away from the observer, orbiting a Sun-like G star in a circular orbit, such that the orbit is oriented in an edge-on fashion. Given an observing geometry, PSG computes the set

⁶ <https://psg.gsfc.nasa.gov>

⁷ <https://github.com/nasapsg/globes>

⁸ <https://goldsmr5.gesdisc.eosdis.nasa.gov/opensap/hyrax/MERRA2/M2I3NVASM.5.12.4/>

⁹ <https://psg.gsfc.nasa.gov/helpapi.php#parameters>

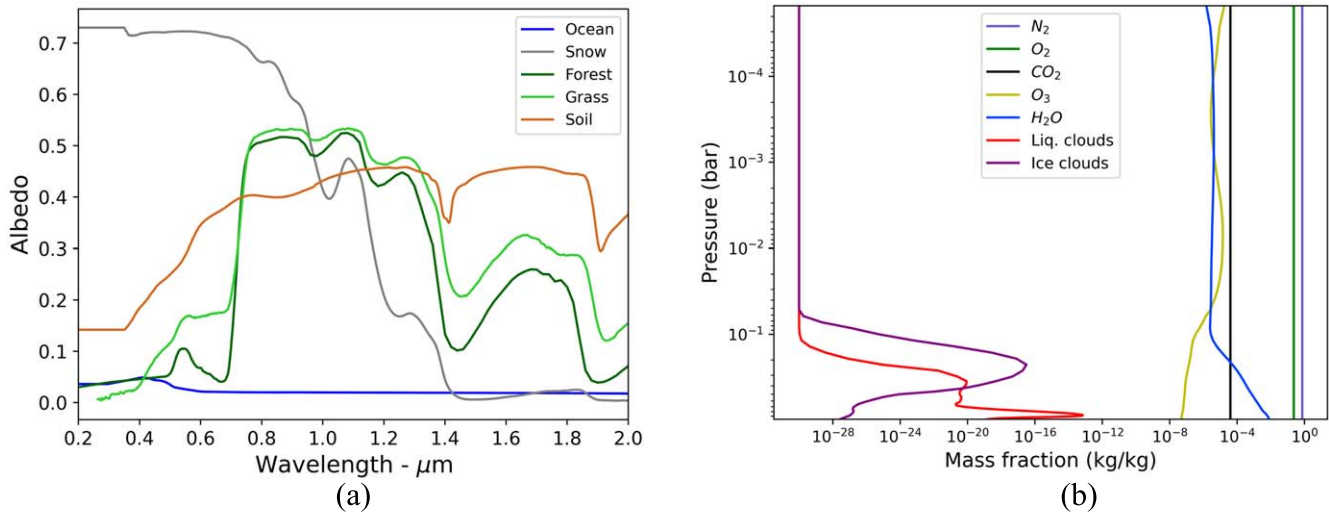


Figure 1. (a) The wavelength-dependent surface albedos of the five surface types—ocean, snow, grass, soil, and forest. The albedo values have been taken from the USGS spectral library (R. Kokaly et al. 2017). The significant increase in the albedos of forest and grass at roughly $0.7 \mu\text{m}$ corresponds to the characteristic vegetation red edge signal, which indicates the presence of surface vegetation. (b) The vertical abundance profiles for the dominant gases and aerosols present in the atmosphere. The abundance of each constituent is denoted by its disk-integrated mass fraction in each layer of the atmosphere. These are modern Earth values derived from the MERRA-2 data corresponding to 2019 March 20th 00:00 UTC.

of incidence and emission angles using a set of sampling algorithms. These angles ultimately inform the radiative transfer codes, which compute the amount of light reflected by the planet at each wavelength (see chapter 2 of the PSG handbook, G. L. Villanueva et al. 2022). The atmosphere is assumed to be in hydrostatic equilibrium and is composed of N_2 , O_2 , CO_2 , CH_4 , N_2O , CO , H_2O , and O_3 along with liquid water and water-ice clouds. The mean vertical abundance profiles of the dominant gases and aerosols are given in Figure 1. N_2 and O_2 , CO_2 , CH_4 , N_2O , and CO are equally distributed throughout the atmosphere with abundances of 78% and 20.9%, 400, 1.6, 1.3, and 0.1 ppmv respectively. H_2O and O_3 are not equally distributed, and their profiles, as shown in Figure 1, are derived from the MERRA-2 data. Similarly, the vertical and horizontal distribution of clouds is derived from the empirical data. In our model, the liquid water and water-ice cloud particles are assumed to have a constant size of 5 and $100 \mu\text{m}$ respectively.

For low-resolution and midresolution simulations, PSG uses correlated k-tables to model the absorption of gases, and these are based on the HITRAN/HITEMP database (L. S. Rothman et al. 2010; I. E. Gordon et al. 2022). These correlated k-opacity tables are precomputed in PSG to make the radiative transfer calculations more efficient. Apart from modeling absorption of gases, we model different atmospheric processes including Rayleigh scattering, refraction, collision-induced absorption, and UV absorption. Rayleigh scattering is computed in PSG following the methodology given in M. Snee & W. Ubachs (2005). PSG uses the refraction indices from <https://refractiveindex.info> to model refraction in the atmosphere, collision induced absorption (CIA) data sets from HITRAN (I. E. Gordon et al. 2022 and references therein) to model CIA, and the MPI-Mainz UV/VIS Spectral Atlas (H. Keller-Rudek et al. 2013) and other UV databases to model UV absorption.

We assume that the surface is Lambertian, and thus, it scatters light isotropically in all directions. For simplicity, we divide the ground coverage into five surface types—ocean, snow, grass, soil, and forest, whose wavelength-dependent

albedos are shown in Figure 1, where the albedo values are taken from the USGS spectral library (R. Kokaly et al. 2017). To compute the disk-integrated flux reflected from the surface, PSG uses the parameters given to describe the observing geometry and the direction of incidence and reflected fluxes. The incidence and reflection angles, along with the albedo of the surface and other parameters, are captured in the bidirectional reflectance distribution function that describes how light from a source is reflected/scattered by an opaque surface. The surface of the planet is not homogeneous, and each of the five surface types has different optical properties. Since we cannot resolve individual surface types, we employ the areal linear mixing model to calculate the effective optical properties of the aggregate. This model assumes that the entire disk is composed of smaller unresolved patches made up of different surface types and that each patch is homogeneous and can be treated separately. The properties of the entire disk like the geometric albedo are simply a linear sum of the individual optical properties of each patch weighted by the corresponding fractional area occupied in the disk.

To perform radiative transfer calculations and accurately simulate spectra, PSG utilizes the Planetary and Universal Model of Atmospheric Scattering, which integrates radiative transfer codes, spectroscopic parameterizations, and correlated-k tables to compute spectra (D. Edwards 1992; M. Wolff et al. 2009; G. Villanueva et al. 2015). Our 3D exo-Earth model is ingested into the GlobES module of PSG where the 3D atmospheric data are mapped onto a 2D observational grid, which is fed to the radiative transfer code. The whole disk is sampled according to the bin size, which is specified in the GCM file. PSG performs the radiative transfer calculations across the whole observable disk, and the disk-integrated spectrum is thus calculated as the linear sum of individual spectra weighted by the projected area of each bin. To consider the effects of Rayleigh scattering and scattering by clouds and other aerosols, the radiative transfer calculations should involve multiple scattering processes. For this purpose, PSG uses the DISORT package, which was specifically developed to efficiently solve the multiple scattering problem

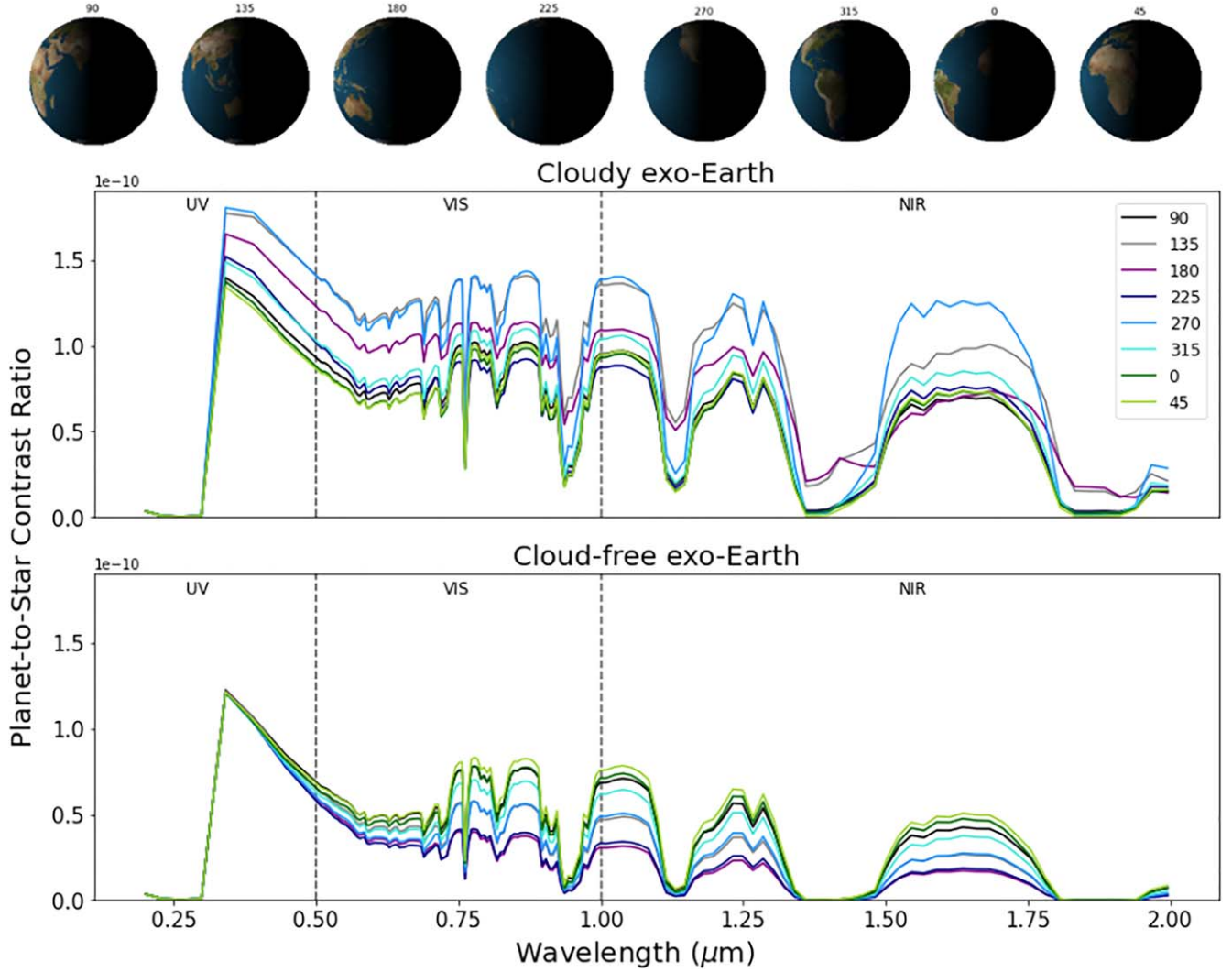


Figure 2. The top panel shows the different rotational configurations of the exo-Earth labeled by a rotational phase. These images only depict how the portion of the surface visible to the observer changes with rotation and do not imply that the planet is cloudless. The plots show the reflected light spectra for the different rotational phases as simulated by PSG for a cloudy and a cloud-free exo-Earth respectively. The entire wavelength bandpass is separated into three regions—(i) ultraviolet (UV) (0.2–0.5 μm), (ii) visible (VIS) (0.5–1 μm), and (iii) near-infrared (1–2 μm). The simulated error bars have been removed for the sake of visual clarity. The cloudy planet shows a higher continuum in the reflected light, which is attributed to the enhanced albedo in the presence of clouds. The spectrum of a cloudy planet also shows a higher degree of variation between rotational phases due to variable cloud patchiness.

(K. Stamnes et al. 1988, 2000; R. Buras et al. 2011). The scattering problem is solved by using a set of numerical approximations, which discretize the differential radiative transfer equation. The number and the size of the discrete equations describing the scattering function can be varied to determine the accuracy of the solution. The number of equations is encoded in “NMAX,” and the size of each equation is given by “LMAX.” For our simulations, we choose NMAX = 1 and LMAX = 66. For more details about the radiative transfer calculations and multiple scattering analysis performed by PSG, refer to chapters 4 and 5 of the handbook (G. L. Villanueva et al. 2022).

2.1. Computing Signal-to-noise Ratios

To calculate the signal-to-noise ratios (SNRs), we adopt a method that has been well established in the literature (J. H. Checlair et al. 2021; R. Kopparapu et al. 2021). To compute the SNR for the detection of any atmospheric constituent, we simulate spectra for two different atmospheric

models: (i) the default model, which includes all atmospheric gases, and (ii) the missing gas model, which includes all gases except one. We take a difference of the spectra simulated using these two models (this is the signal) and divide it by the noise simulated by PSG (see chapter 8 of the PSG handbook, G. L. Villanueva et al. 2022) to get the SNR at each wavelength. The net SNR can be calculated as a square root of the sum of squares of individual SNRs at each wavelength.

$$\text{netSNR} = \sqrt{\sum_i (\text{SNR})_i^2}.$$

3. Results

3.1. Spectra of a Rotating and Revolving Exo-Earth

We simulate observations of the planet at quadrature, where it is at the maximum angular separation from the star, and well outside the inner working angle (IWA) of the coronagraph. We choose a random day (2000 July 1) from MERRA-2’s historical record and construct our atmospheric model based

on empirical data obtained on that day. We also looked at other days, and based on the cloud distribution on any given day, we observed a similar trend in the spectra, and hence, we only present results for one case.

Figure 2 shows the simulated spectra of a rotating planet where each rotational configuration is labeled by a rotational phase. Each rotational phase is separated by 3 hr to match the temporal resolution of the MERRA-2 atmospheric data. At each phase, we update our atmospheric model with new empirical data to ensure that our model accurately replicates the dynamic atmospheric conditions prevalent on Earth. Figure 2 shows the simulated reflected light spectra in three wavelength bands—UV, visible (VIS), and near-infrared (NIR) for the different rotational phases labeled in the top panel. The range of the wavelength bands is adopted according to the recommendations of the LUVOIR mission report (LUVOIR Team 2019). The cloudy planet’s spectrum shows significant variation over a short span of 24 hr, and this dynamic nature of the spectrum is primarily attributed to the variability in cloud cover over different parts of the disk. This is similar to what has been observed on Earth with DSCOVR (L. Gu et al. 2021) and in other exo-Earth studies (V. Kofman et al. 2024). This variation is highly apparent in between $0.3\text{--}0.7\text{ }\mu\text{m}$ and $1.5\text{--}1.8\text{ }\mu\text{m}$. The spectra of a cloudy planet show at max a $\sim 75\%$ variation in reflected flux at $0.5\text{ }\mu\text{m}$ for different rotational phases. In contrast, the cloud-free spectra only vary by $\sim 15\%$ at the same wavelength, due to the changing surface albedo. Extensive cloud cover over the eastern Pacific Ocean (phase 270) and parts of South and Southeast Asia (phase 135) significantly enhances the reflected light continuum at these phases. In contrast, the dearth of clouds over Africa (phase 45) and the western Atlantic Ocean (phase 0) leads to a much lower reflectance. In the absence of clouds, the reflected light continuum shifts to a lower value as the surface has a lower albedo than the clouds. Additionally, the spectra show less variation, attributed now only to the changing surface albedo.

We also compare the reflected light spectra of both a cloudy and a clear planet at three different orbital phases—quadrature (Q) and $Q \pm 30^\circ$, ensuring that the planet is outside the IWA of the coronagraph. For these simulations, the exposure time is set to 24 hr. Since the MERRA-2 data collection has a temporal resolution of 3 hr, we combine eight data files corresponding to a single day (2000 July 1), and take an average of the atmosphere and surface data to construct our exo-Earth model. This is done to replicate a real 24 hr observation, in which, the instrument would receive light reflected by different parts of the planet’s disk as it rotates. The collected photon data would represent an integrated disk “averaged over” each rotational configuration. Considering both a cloudy and a clear planet, the spectra show a $\sim 30\%\text{--}100\%$ variation in spectra at $0.5\text{ }\mu\text{m}$ between subsequent orbital phases. This is comparable to the variations seen in the spectra of a rotating cloudy planet. The spectra show a lower percentage of variation at higher wavelengths (for, e.g., $\sim 25\%\text{--}40\%$ variation at $1\text{ }\mu\text{m}$), which implies that the scattering and reflection by clouds in the visible band enhance the changes in spectra at different orbital phases.

3.2. The Impact of Clouds on SNRs of Atmospheric Gases

The previous section shows that clouds have a significant impact on the reflected light spectrum of the integrated disk as well as on the absorption signals of different gases. By extension, we explore their impact on SNRs of these gases in

this section. We restrict our analysis to O_2 , O_3 , and H_2O because (i) they have strong absorption lines in the considered wavelength bands, and moreover, (ii) they are important biomarkers. Figure 3 shows the wavelength-dependent SNRs of these three gases for a cloudy and cloud-free exo-Earth, as computed assuming a 6 m HWO telescope PSG template with a suitable noise model and a 24 hr exposure. The instrumental parameters of this template are given in Table 1 and Figure 7. Clouds enhance the SNRs of all the three gases across the considered wavelength range. Since the same noise model is employed for the cloudy and the cloud-free case, the subsequent increase in SNRs is due to an increase in the strength of absorption signals in the presence of clouds, which is attributed to their greater (than the surface) albedo. Since it is difficult to probe the atmosphere below a cloud layer, for clouds to boost the absorption signals of these gases, they should be present in significant quantities above the cloud layer. Hence, the vertical abundance of each gas with respect to the clouds also influences the SNR values. O_3 is abundant in the stratosphere, much higher than a large fraction of the clouds, while O_2 is well mixed throughout the atmosphere, and H_2O is abundant in the troposphere. Even though H_2O abundance reduces with height, a significant fraction of the gas is still present above the layer of liquid clouds (see Figure 1). Optically thick clouds in the lower altitude regions of the troposphere have a huge impact on the SNRs of O_2 and H_2O , enhancing them by almost a factor of 2 (e.g., the O_2 absorption line at $0.76\text{ }\mu\text{m}$). Higher up in the troposphere, the clouds get optically thinner, and thus, their impact on the SNRs of O_3 is not that significant (~ 11 for a cloud-free case to ~ 15 for a cloudy case at $0.3\text{ }\mu\text{m}$). The O_2 signature in the UV band might be a computational artifact caused by imprecise modeling of the Rayleigh tail, but we are still investigating the exact reason. Nevertheless, this does not significantly affect our results as O_2 absorbs primarily in the visible band where observations should be directed.

Thus, the presence of cloud cover impacts whether a robust detection of an atmospheric signal can be made within a reasonable exposure time. For example, a 24 hr long exposure is not enough to achieve net $\text{SNR} = 5$ for H_2O on a cloudless planet, but for a cloudy planet, the same exposure yields a net $\text{SNR} > 5$. For both the cloudy and the cloud-free exo-Earth, comparing the net SNRs shows that O_3 is the easiest to detect followed by H_2O and then O_2 . However, this is assuming that the instrument has a full bandpass and can simultaneously observe in all three wavelength bands. This might not be true for future missions with disparate wavelength coverage and narrow bandpasses. In this case, O_2 is the most promising candidate for detection as it has strong absorption line in the visible band. O_3 and H_2O have broad absorption signals and may require multiple passes for a robust detection. We observe similar trends when considering other days as well, and hence, this signal enhancement is not affected by the chosen day.

3.3. The Impact of a Global Cloud Layer at Different Pressure Levels

In this section, we explore the impact of a global cloud layer at different altitudes/pressure levels on the reflection spectra and the detectability of atmospheric gases. Similar work has been done before using 1D climate models (Y. Kawashima & S. Rugheimer 2019), and we complement their results using a 3D empirical exo-Earth model. The thickness of the global

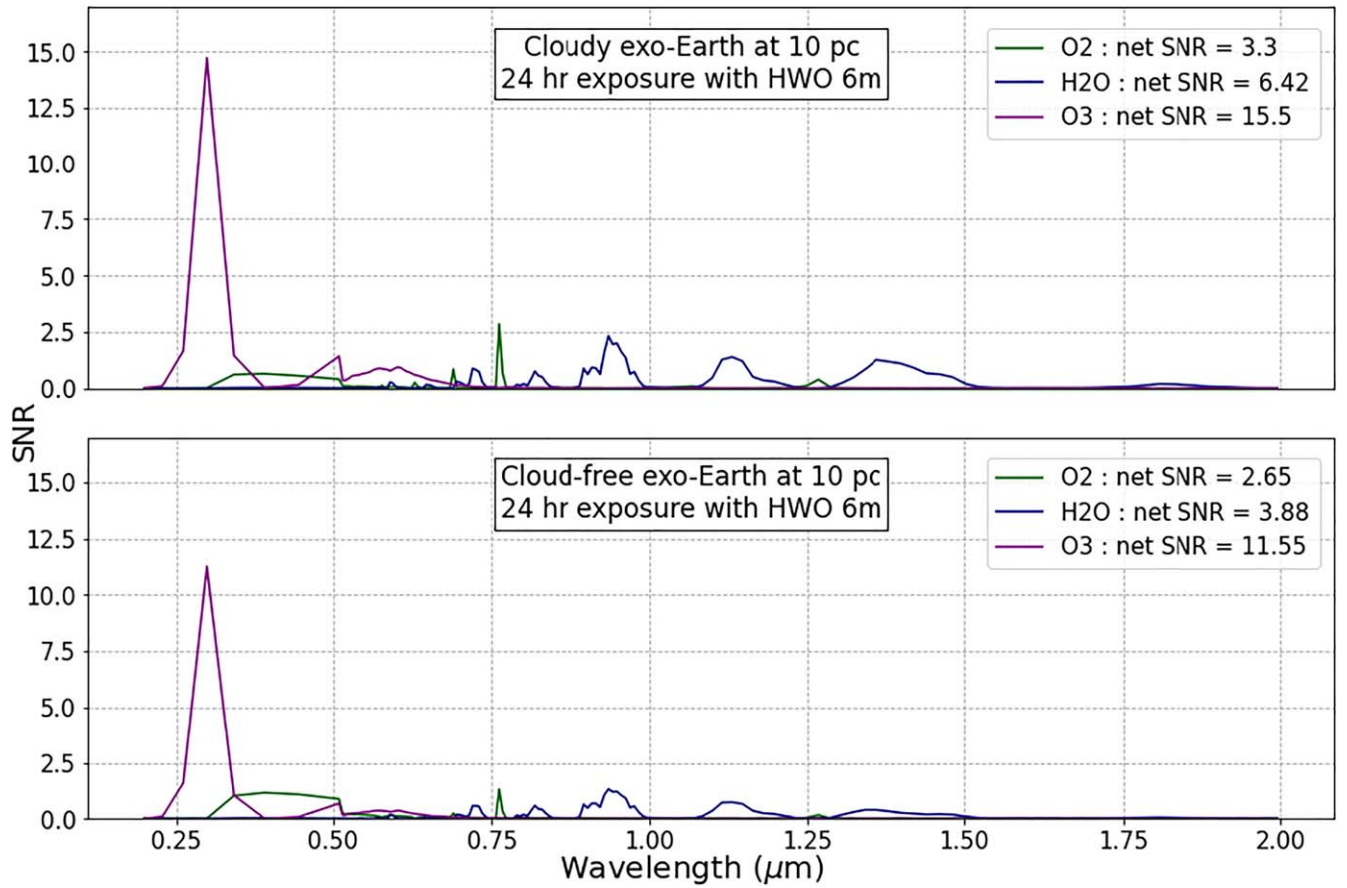


Figure 3. The wavelength-dependent SNRs of the three gases, O_2 , O_3 , and H_2O . The top panel shows the results for a cloudy exo-Earth while the bottom panel depicts the same for a cloud-free exo-Earth. The simulations are performed in PSG using a 6 m HWO template and a suitable noise model assuming that the exo-Earth is situated 10 pc away, and the exposure time is set to 24 hr. The corresponding net SNRs for each gas across the entire wavelength region is given in the legend. Clouds enhance the SNRs of all the three gases and hence improve their detectability in an exo-Earth atmosphere. The increase in SNR for each gas is dependent on its vertical distribution with respect to the distribution and opacity of patchy clouds.

cloud layer is kept constant in the pressure space (0.1 bar), and we consider four cases where this cloud layer is placed between different pressure levels in the atmosphere—(i) 0.8–0.7 bar, (ii) 0.48–0.38 bar, (iii) 0.34–0.24 bar, and (iv) 0.18–0.08 bar. These are arbitrary pressure levels chosen according to the constraints of the 3D structure of the MERRA-2 data, but we still try to sample the entire extent of the troposphere. The first three cases correspond to liquid water cloud layers while the last case corresponds to a water-ice cloud layer, since temperatures between those pressure levels are low enough to form ice crystals. The cloud layer is “constructed” by converting all the gaseous water vapor in between the two pressure levels to cloud condensates. This conversion is done in two different ways—(i) we take a spatial average of the water vapor abundance (quantified by the water vapor mass fraction as given by the MERRA-2 data) over all latitudes and longitudes between the two pressure levels and convert this to a cloud mass fraction, or (ii) we divide the globe into 10° latitude bins, and in each bin, we take a spatial average of the water vapor mass fraction over all longitudes and latitudes and convert this to a cloud mass fraction, all within that bin. This is done to incorporate the spatial differences in water vapor over different parts of the globe. However, we find that the results of these two cases are nearly similar, since we cannot resolve spatial differences in cloud cover when the exo-Earth is 10 pc

away. Thus, we only present results corresponding to the first case, with no latitudinal binning.

The top panel of Figure 4 shows the reflectance spectra for an exo-Earth with a global cloud layer between four different pressure levels, as described above, with a clear sky spectrum also plotted for reference. The amount of water vapor decreases as we go to higher altitudes/lower pressures, and subsequently, the cloud layers become optically thinner. Thus, the reflected light continuum decreases as the altitude of the global cloud layer increases, but the continuum for all four cases is higher than the clear sky continuum. As mentioned before as well, the depth of the gaseous absorption signals is highly dependent on the distribution of clouds with respect to the vertical abundance of the gas. In addition to this, the water vapor absorption bands are also a function of how much water vapor has been converted to clouds between the considered pressure levels.

The middle and bottom panels depict the SNRs of (i) O_2 in the visible band, (ii) O_3 in the UV band, and H_2O in the (iii) visible and (iv) NIR band, with the net SNRs in the corresponding band given in the legend. For O_2 , a zoomed-in plot depicting the two prominent absorption lines in the visible band is shown; however, the net SNRs are computed for the entire visible band. O_2 is a well-mixed gas and is present throughout the atmosphere with a constant mixing ratio of ~ 0.21 . Low-lying and optically thick clouds significantly enhance the SNR for O_2 (compared to a clear sky) since a large

Table 1
The Parameters that Describe the Instrumental Configuration for the Four Mission Concepts, LUVOIR A/B, Habex with SS, and HWO

Parameter	LUVOIR-A	LUVOIR-B	Habex/SS	HWO
Diameter	15 m	8 m	4 m	6 m
Spectral range	UV: 0.2–0.515 μm VIS: 0.515–1 μm NIR: 1–2 μm	UV: 0.2–0.515 μm VIS: 0.515–1 μm NIR: 1–2 μm	UV: 0.2–0.45 μm VIS: 0.45–0.975 μm NIR: 0.975–1.8 μm	UV: 0.2–0.515 μm VIS: 0.515–1 μm NIR: 1–2 μm
Resolving power (RP)	UV: 7 RP VIS: 140 RP NIR: 70 RP	UV: 7 RP VIS: 140 RP NIR: 70 RP	UV: 7 RP VIS: 140 RP NIR: 40 RP	UV: 7 RP VIS: 140 RP NIR: 70 RP
Exozodi level	4.5	4.5	4.5	4.5
Contrast	1×10^{-10}	1×10^{-10}	1×10^{-10}	1×10^{-10}
IWA	4 λ/D	3.5 λ/D	UV: 39 mas VIS: 58 mas NIR: 104 mas	3.5 λ/D
Read noise	UV: 0 VIS: 0 NIR: 2.5	UV: 0 VIS: 0 NIR: 2.5	UV: 0.008 VIS: 0.008 NIR: 0.32	UV: 0 VIS: 0 NIR: 2.5
Dark noise	UV: 3×10^{-5} VIS: 3×10^{-5} NIR: 0.002	UV: 3×10^{-5} VIS: 3×10^{-5} NIR: 0.002	UV: 3×10^{-5} VIS: 3×10^{-5} NIR: 0.005	UV: 3×10^{-5} VIS: 3×10^{-5} NIR: 0.002

Note. Parameter values adapted from the respective final reports. We assume that the HWO has the same instrumental parameters as LUVOIR-B, except for a smaller mirror size.

fraction of O_2 is present above the cloud layer and contributes to absorption, and moreover, the optically thick clouds increase the reflectivity of the disk. As the altitude of the cloud layer increases, it gets difficult to probe the atmosphere below the cloud layer, and thus, the amount of O_2 contributing to the absorption signal reduces, which leads to a reduction in the SNR. O_3 is mainly abundant in the stratosphere, below the pressure levels being considered here, so the only impact of a cloud layer at higher pressures is to increase the reflectivity of the disk. As the altitude of the cloud layer increases, the clouds become optically thinner and less reflective, leading to a reduction in the SNRs for O_3 . Water vapor is not a well-mixed gas and, moreover, is also converted to cloud condensates between the pressure levels considered. These two factors contribute to the trend seen in the SNRs of H_2O in the visible and the NIR band. We conclude that a low-lying optically thick cloud layer can significantly enhance the SNRs of well-mixed atmospheric constituents and thus reduce the exposure times required to make a robust detection. For O_2 and H_2O , the altitude of the global cloud layer dictates whether a 24 hr exposure yields net SNRs ≥ 5 .

3.4. The Impact of Naturally Varying Cloud Cover

In the previous sections, we quantified the effects of clouds by comparing atmospheres with the explicit presence and the absence of clouds as well as clouds at different altitudes in the atmosphere. In this section, we explore the impacts of the amount of cloud abundance on the reflectance spectra and the detectability of gases. The amount of cloud coverage is a highly variable quantity, impossible to predict and highly dependent on climate and weather variability. The amount of cloud coverage can change significantly over different timescales, and it is important to accurately quantify the impacts of these changes. Similar to Earth, we expect other terrestrial habitable

worlds to have short-term weather patterns and long-term climate cycles resulting in a dynamic atmosphere, which might impact the detectability of atmospheric constituents.

We go through the MERRA-2's historic cloud data record to identify trends in cloud variability over different timescales. We specifically use MERRA-2 data, which gives us simulated clouds, instead of other data sets with observed cloud data, like ISCCP (A. H. Young et al. 2018) or CERES (N. G. Loeb et al. 2018)) for the following reasons: (i) the MERRA-2 data are 3D, and thus, the cloud data can be easily incorporated into our 3D exo-Earth model, (ii) MERRA-2 uses a cloud mass fraction, in addition to cloud coverage as a proxy for a cloud abundance. This cloud mass fraction is essential for a radiative transfer calculation, and it can be used to calculate an effective mass of cloud particles in the atmosphere. We find that a comparison between different data sets (for e.g., MERRA-2 and ISCCP) is impractical because (i) the MERRA-2 data are 3D while the ISCCP data are 2D, and (ii) both data sets use different proxies for quantifying cloud abundances. The MERRA-2 pipeline simulates the cloud mass fraction and the areal cloud coverage at different layers in the atmosphere while the ISCCP algorithm converts the observed reflected radiance to top-of-the-atmosphere areal cloud coverage. A combination of simulated and observed cloud abundances might have yielded more accurate trends; however, we find that such a combination is not possible because of the different proxies employed. A more detailed comparison is needed to accurately integrate different data sets; however, that is outside the scope of this work.

We use the cloud mass fraction given by the MERRA-2 data to compute an effective global cloud mass. For an exo-Earth situated 10 pc away, we cannot resolve clouds at local scales and hence use this effective global cloud mass as a measure of global cloud abundance. Considering one column (lat \times lon), we compute the pressure-weighted cloud mass fraction

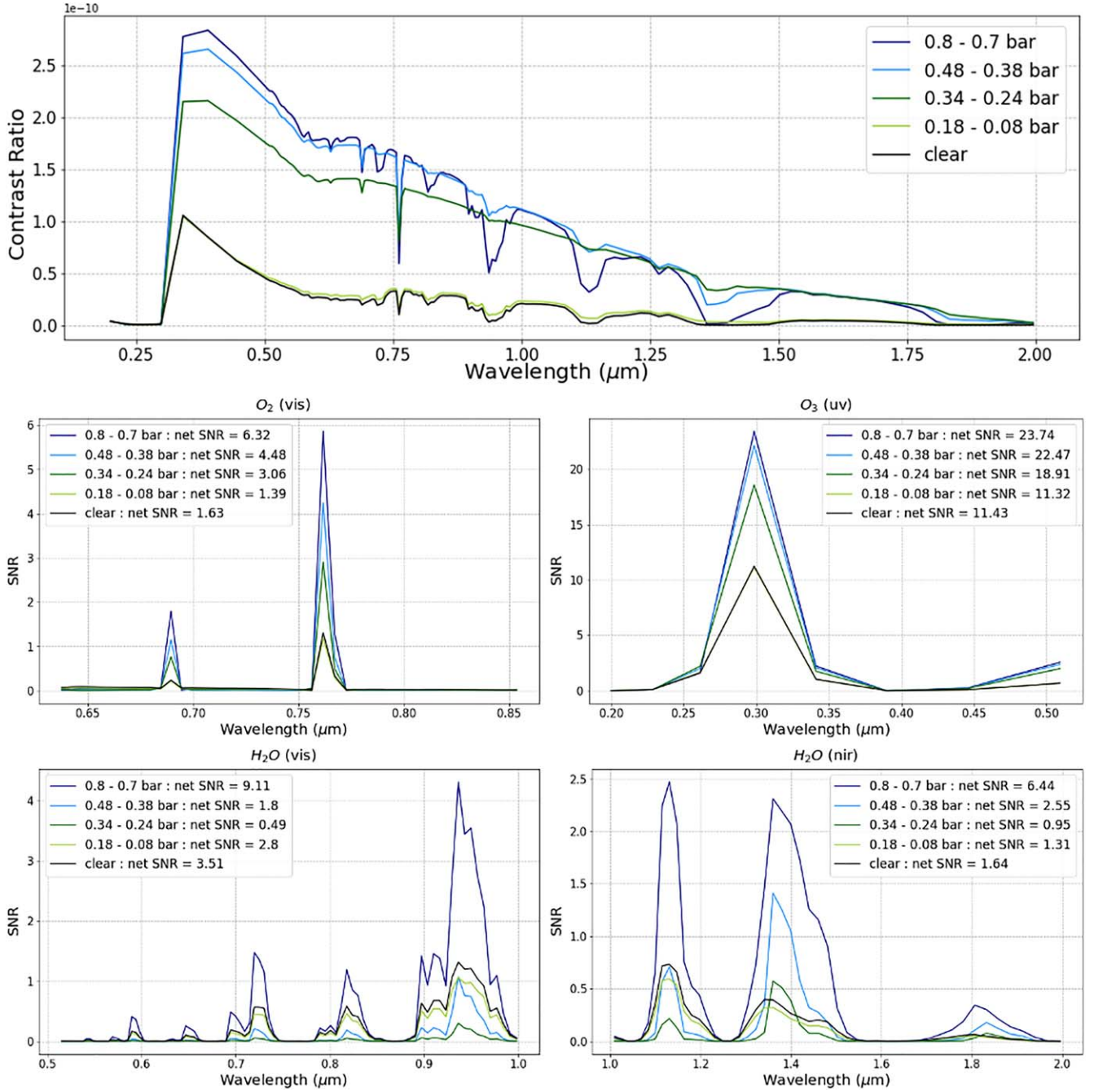


Figure 4. A global cloud layer of constant 0.1 bar thickness is considered at four different pressure levels—(i) 0.8–0.7 bar, (ii) 0.48–0.38 bar, (iii) 0.34–0.24 bar, and (iv) 0.18–0.08 bar. The top panel shows the reflectance spectra for these four cases with a clear sky spectrum plotted for reference. As before, these simulations are done with a 6 m HWO template with an exposure time of 24 hr for a planet that is 10 pc away. The middle panel shows the SNRs of O_2 in the visible band and O_3 in the UV band, and the bottom panel shows the SNRs of H_2O in the visible and NIR band. As the altitude of the cloud layer increases, the clouds become optically thinner, and thus, their reflectivity reduces leading to a lower continuum in the reflected light spectrum. The trends seen in the SNRs of all the three gases is a reflection of how they are distributed with respect to the global cloud layer.

throughout that column or the liquid water path (LWP) as

$$\text{LWP (in } \text{kgm}^{-2}) = \int_{P_s}^0 m_c \frac{dP}{g} \quad (1)$$

where P_s is the surface pressure, m_c is the cloud mass fraction in each layer, and g is the acceleration due to gravity. The area of a grid centered around latitude λ and longitude ϕ is given by

$$A = r_{\oplus}^2 \cos(\lambda) d\lambda d\phi. \quad (2)$$

According to the resolution of the MERRA-2 data, $d\lambda = 0.5^\circ$ and $d\phi = 0.625^\circ$ everywhere on the grid. Multiplying the LWP with the area of the grid gives an effective cloud mass for one column. Taking a spatial average of this effective mass over all the columns gives the effective global cloud mass (in kilograms).

The MERRA-2 data collection M2I3NVASM contains atmospheric data from 1984—present, with a temporal resolution of 3 hr, and hence, it would be computationally

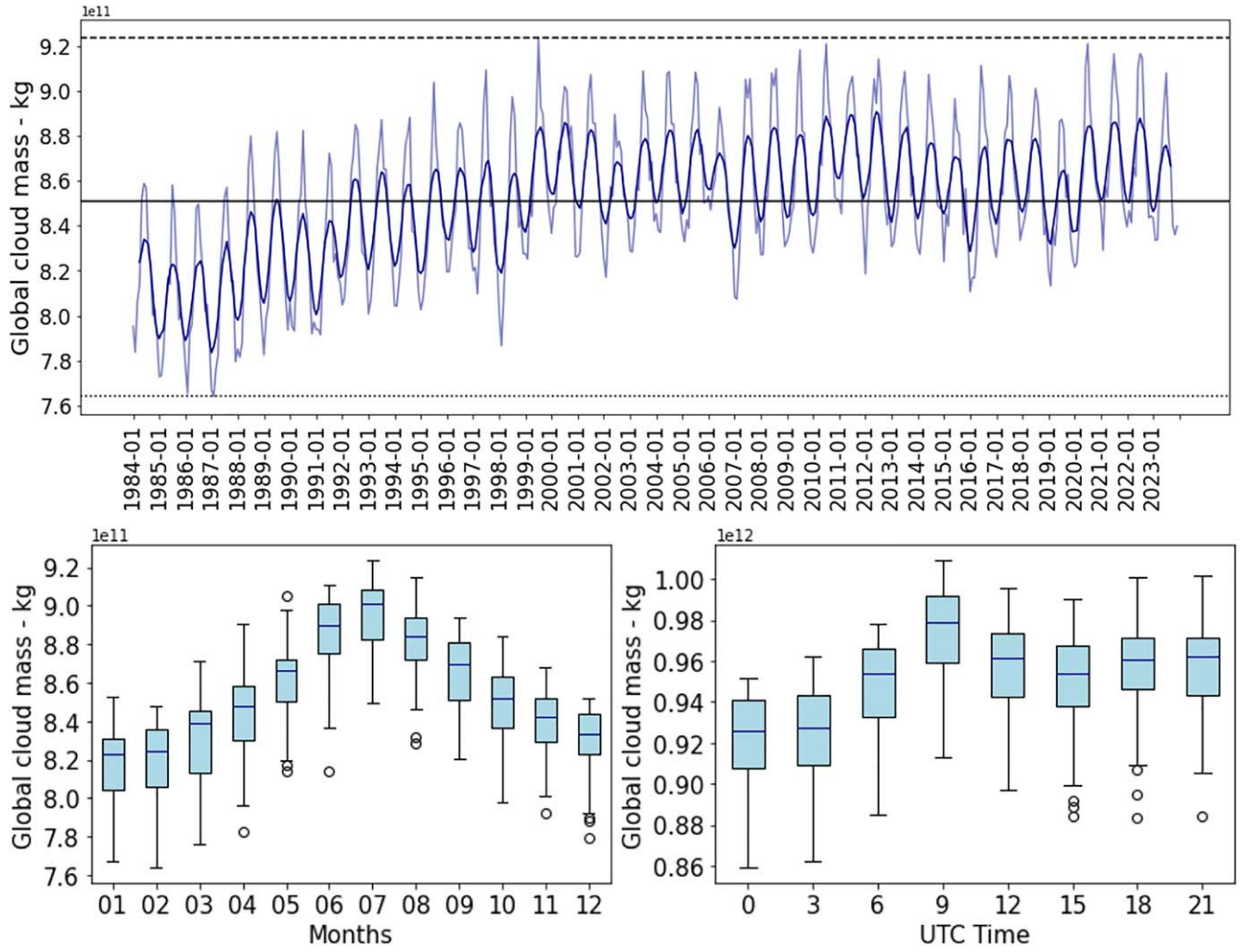


Figure 5. The top panel shows the evolution of the monthly averaged global cloud mass across MERRA-2’s historic record from 1984 to 2023. The dashed and the dotted lines represent the maximum and minimum of the data, which correspond to the months of 1999 July and 1987 February respectively. The solid line represents the mean, which is closest to the 2011 January monthly averaged data. The faint blue curve represents the actual data while the dark blue curve is the rolling average over a window of 7 months. The bottom panels depict trends in cloud cover variability over seasonal and diurnal timescales. The left panel shows the trends in global cloud mass across a year, and the boxes have been constructed using monthly averaged data from 1984 to 2023. The right panel depicts the diurnal trend, and the boxes are plotted using instantaneous 3 hr data for all days in the month of 1999 July. For both these panels, the dark blue line represents the median, the edges of the box extend from the first quartile (Q1) to the third quartile (Q3), the whiskers extend to the farthest data points within 1.5 times the interquartile range (Q3–Q1) from the box, and the outliers are data points beyond this range.

intensive to go through all that data and identify trends in cloud cover. MERRA-2 also has a separate collection M2TMNPCLD (Global Modeling and Assimilation Office (GMAO) 2015b) that offers monthly averages of cloud data, which we utilize to compute the monthly averaged effective global cloud mass from the years 1984–2023. Using the global cloud mass as a proxy, we identify the trends in global cloud cover at different timescales. The top panel of Figure 5 shows the evolution of the global cloud mass across 1984–2023, where each data point represents a monthly average. The data show evidence for an overall increase in the global cloud mass over the past few decades. The bottom left panel shows the seasonal cloud variability across a year. The boxes are drawn using the monthly averaged data from 1984 to 2023, where the median is depicted by the dark blue line. Cloud mass increases during the Northern summer months, peaking in July, and then reduces during the winter months. All the months show a $\sim 5\%$ – 10% variation in the monthly averaged cloud mass across the considered time period. For half the months, there are no

outliers, and all data lie within the whiskers while the rest of the months show one to three outlier data points. This seasonal variability also underlies the long-term trend seen in the top panel. From these data, we identify the months corresponding to the highest, lowest, and the mean global cloud mass (given by the dashed, solid, and dotted lines respectively). 1999 July shows the highest monthly averaged global cloud mass— 9.24×10^{11} kg—while 1987 February has the lowest cloud mass— 7.64×10^{11} kg. The mean cloud mass values of 8.5×10^{11} kg is closest to the 2011 January data. Finally, the bottom right panel shows the diurnal cloud variability across the cloudiest month of 1999 July. These boxes are plotted using data from the 3 hr data collection M2I3NVASM. The diurnal variation is not significant, and there are only a few outliers.

Having identified the months corresponding to the highest and the least monthly averaged global cloud mass, we use the 3 hr data collection M2I3NVASM to compute the global cloud mass across all the days in those months and identify the days with the highest (July 7) and the lowest (February 15) cloud

cover. Here, we have made the assumption that the month with the highest monthly averaged global cloud mass will have days with relatively high global cloud mass and vice versa, and thus, we understand that these might not be the days with the absolute highest or lowest global cloud mass across MERRA-2's historic record. However, in the relative sense, these days can be classified as days with high and low cloud abundance respectively. Similarly, we also identify the day (2011 January 20th) with the global cloud mass closest to the mean cloud mass across the historic record. We subsequently construct our exo-Earth atmospheres using empirical cloud data from these dates and analyze the impact of the amount of cloud cover on planetary spectra and SNRs of atmospheric gases. Note that, instead of identifying individual days, we could have simply used the monthly averaged cloud data to construct our atmosphere, but we did not do so for two reasons—(i) the 3D structure of the monthly averaged data collection is different, it has 42 atmospheric layers, instead of the 72 layers in the 3 hr data collection, and (ii) analyzing data from individual days might reveal outliers with high weightage in the monthly average, and this would yield a more dramatic comparison.

The top panel of Figure 6 shows the reflectance spectra for exo-Earth atmospheres constructed using MERRA-2 data from the following dates—1999 July 7, 2011 January 20, and 1987 February 15. These cases are respectively labeled as high, mean, and low, pertaining to the level of cloud abundance. A clear sky spectrum is also plotted for reference. The cloudy spectra show differences in the reflected light continuum, which is attributed to the differences in the amount of cloud abundance and the subsequent disk albedo. These differences are prominent in the visible band where scattering and reflection by clouds are dominant. The spectra show a maximum variation of $\sim 15\%$ at $0.5 \mu\text{m}$, which is much lower than the variations exhibited by a generic cloudy planet at different orbital phases. The middle and bottom panels depict the SNRs of atmospheric constituents O_2 , O_3 , and H_2O . O_2 is a well-mixed gas, and thus, an increase in the amount of cloud abundance and the subsequent albedo increases the SNRs. O_3 is dominant in the stratosphere, and thus, differences in tropospheric cloud coverage do not significantly alter its detectability. The SNRs of H_2O also scale with cloud abundance with high cloud abundances leading to higher SNRs. Note that this scaling is due to an increase in the albedo for higher cloud abundances and not because of an increased absorption by water cloud condensates. These condensates absorb at much higher wavelengths in the infrared (resulting in the greenhouse effect), which is not relevant here as this is beyond our considered wavelength bands. We conclude that atmospheres with higher cloud abundance increase the detectability of the atmospheric gases considered here and also reduce the exposure times required to make robust detections of these gases. This is especially highlighted by comparing the net SNRs of H_2O in the visible band. Setting a threshold of $\text{SNR} = 5$, it is evident that 24 hr is not enough to make a robust detection of H_2O in the visible band for an atmosphere with low cloud abundance. Meanwhile, atmospheres with mean and high cloud abundances result in net SNRs > 5 .

We note that, even though the data used to construct the cloud distributions considered here span several decades, the differences presented in Figure 6 are not meant to be representative of variations on observationally relevant

timescales. We simply take advantage of MERRA-2's rich historical record to find periods with significant differences in cloud amount and use the subsequent empirical data to construct realistic cloud distributions on an exo-Earth. It is impossible to have any prior information on the amount of cloud abundance, and hence, during an observation, an exo-Earth might be highly cloudy, less cloudy, or somewhere in between the two extremes. Figure 6 shows the possible variations in spectra and atmospheric detectability for an exo-Earth with variable cloud abundance and highlights the fact that it is difficult to establish a stable atmospheric baseline in the presence of clouds.

For cases when we do not have access to the full reflection continuum (for example, if observations are restricted to certain bandpasses), our analysis also highlights a possible degeneracy between the amount of cloud abundance and the abundance of an atmospheric gas while interpreting observed SNRs. For, e.g., an atmosphere with a high cloud abundance and low O_2 concentration might yield the same SNRs as an atmosphere with high O_2 concentration but low cloud abundance. Exploring this degeneracy in detail and possible solutions to resolve it requires an in-depth analysis using photochemical modeling and retrievals, which is outside the scope of this study.

3.5. Comparison between Different Mission Concepts

In this section, we do a comparative analysis of future direct-imaging mission concepts—(i) LUVUOIR-A (15 m), (ii) LUVUOIR-B (8 m), (iii) HWO (6 m), and (iv) Habex with starshade (Habex-SS) (4 m), in investigating the impacts of clouds. We use PSG to simulate all our observations with these instruments, and all the instrument parameters, as shown in Table 1, are taken from the respective final reports (LUVUOIR Team 2019; B. S. Gaudi et al. 2020). Since the HWO report is still under development, we consider the HWO instrument parameters to be the same as the LUVUOIR-B parameters, except with a smaller mirror size. The coronagraphic planetary throughput and the optical throughput of each instrument are shown in Figure 7. For a detailed discussion on the throughputs and the PSG noise model, refer to J. H. Checlair et al. (2021) or the PSG handbook (G. L. Villanueva et al. 2022).

We simulate observations with all the instruments considering that our exo-Earth is placed 10 pc away, situated at quadrature and set our exposure times to 24 hr. As described above, we take an average of the atmospheric data over all parts of the disk to represent the observation of an integrated disk. We compute the individual wavelength-dependent SNRs and the bandwise net SNRs of the three gases— O_2 , H_2O , and O_3 . Following the method given in J. H. Checlair et al. (2021), we then calculate the exposure times required to achieve $\text{SNRs} = 5$.

$$t_{\text{exp}} = 24(\text{hr}) \times \left(\frac{5}{\text{SNR}} \right)^2. \quad (3)$$

For this comparison, we consider six types of atmospheres—an atmosphere having patchy clouds with (i) high, (ii) mean, and (iii) low cloud abundance, an atmosphere with global cloud coverage with clouds between two pressure levels, (iv) 0.8–0.7 bar, and (v) 0.34–0.24 bar, and a (vi) clear atmosphere with no clouds. The atmospheres with varying cloud abundances are constructed using empirical MERRA-2 data corresponding to those dates, as described in the previous

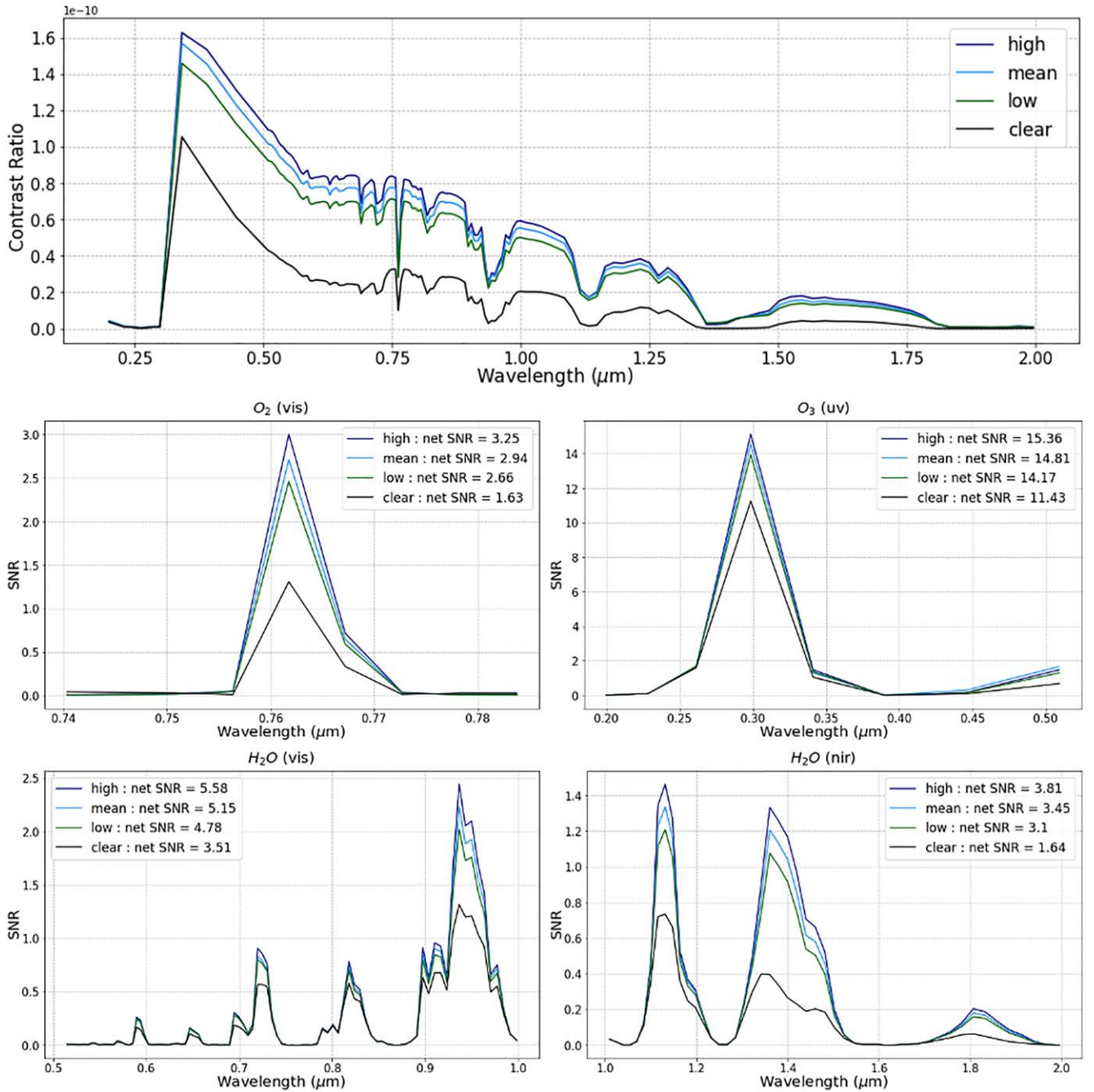


Figure 6. A comparison of the spectra and gaseous SNRs for an exo-Earth with varying amounts of cloud abundance. The high, mean, low cloud abundance labels correspond to exo-Earth atmospheres constructed using MERRA-2 data from the dates 1999 July 7, 2011 January 20, and 1987 February 15 respectively. A clear sky scenario is also shown for reference. The simulations are done with a 6 m HWO template with an exposure time of 24 hr considering that the planet is 10 pc away and placed at quadrature. The reflected light continuum and the atmospheric SNRs increase with cloud abundance.

section. To compute these SNRs and exposure times, we consider the strongest absorption lines/bands—(i) the O_2 A line at $\sim 0.76 \mu\text{m}$ in the visible band, (ii) the H_2O absorption band across $0.9\text{--}1 \mu\text{m}$ in the visible band, (iii) the H_2O absorption band across $1.25\text{--}1.6 \mu\text{m}$ in the NIR band, and (iv) the O_3 absorption band across $0.2\text{--}0.4 \mu\text{m}$ in the UV band.

For the absorption bands, we compute the net SNR across the range of absorption and then ingest this net SNR into the equation above to calculate the exposure time. Tables 2, 3, 4, and 5 depict the exposure times required to make a robust detection defined by setting a threshold $\text{SNR}=5$ for all the six atmospheres described above considering four future direct-

imaging mission concepts. As shown in Table 1 and Figure 7, the main differences between these mission concepts that affect the exposure time computations are the instrument mirror size and the instrument throughputs. The instrumental noise increases with reducing mirror size causing a subsequent increase in the required exposure times. Thus, LUVOIR-A with the largest mirror size of 15 m shows the highest performance and yields the lowest exposure times for all absorbing gases. It is followed by LUVOIR-B with an 8 m big primary mirror. However, Habex-SS (4 m) performs better than HWO (6 m) due to its superior planetary and optical throughput (see Figure 7) in spite of a smaller mirror size.

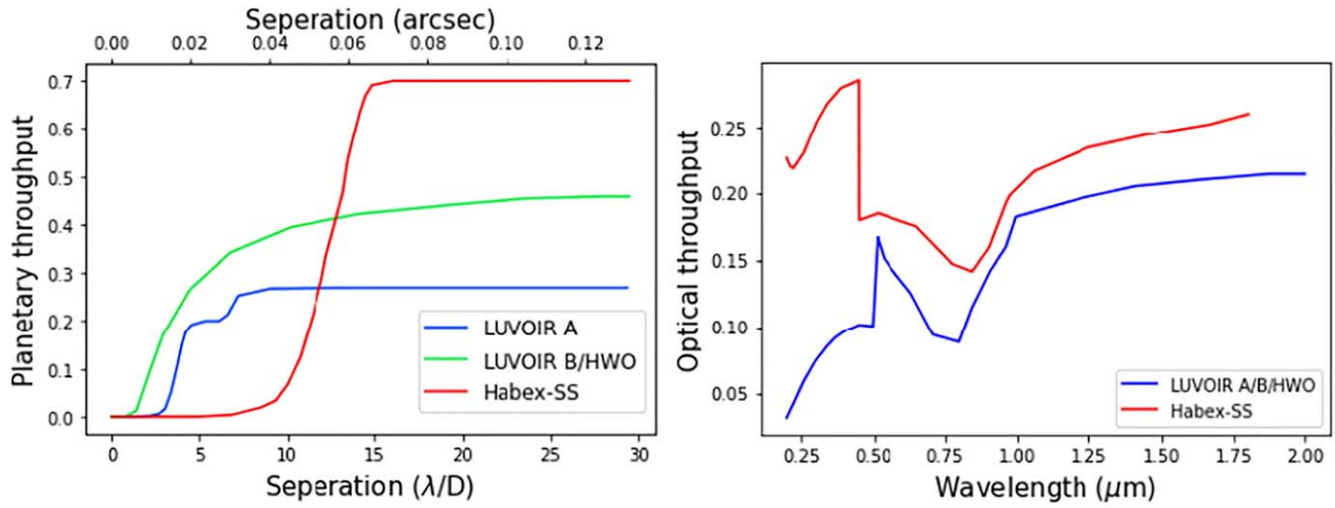


Figure 7. The planetary and optical throughputs for all the four instruments considered for the comparison.

Table 2

The Exposure Times Required to Make a Robust Detection ($SNR = 5$) of the O_2 A Line for the Six Types of Atmospheres Described Above for an Exo-Earth at 10 Pc Away Placed at Quadrature in Its Orbit

Type of Atmosphere	LUVOIR-A (hr)	LUVOIR-B (hr)	HWO (hr)	Habex-SS (hr)
Patchy clouds with high cloud abundance	2.4	18.24	66.54	63.79
Patchy clouds with mean cloud abundance	2.91	22.33	81.62	78.32
Patchy clouds with low cloud abundance	3.49	27.05	99.13	95.32
Global cloud layer from 0.8–0.7 bar	0.73	4.97	17.47	16.31
Global cloud layer from 0.34–0.24 bar	3.23	20.7	71.17	65.68
No clouds	10.94	93.14	350.65	343.02

Table 3

The Exposure Times Required to Make a Robust Detection ($SNR = 5$) of the H_2O 0.9–1 μm Absorption Band for the Six Types of Atmospheres for an Exo-Earth Placed 10 Pc Away at Quadrature

Type of Atmosphere	LUVOIR-A (hr)	LUVOIR-B (hr)	HWO (hr)	Habex-SS (hr)
Patchy clouds with high cloud abundance	0.59	5.43	22.34	16.77
Patchy clouds with mean cloud abundance	0.69	6.36	26.21	19.68 hr
Patchy clouds with low cloud abundance	0.8	7.47	30.95	23.16
Global cloud layer from 0.8–0.7 bar	0.26	2.08	8.23	6.08
Global cloud layer from 0.34–0.24 bar	94.6	692.12	2645.57	1992.9
No clouds	1.3	13.81	59.05	44.35

For a given instrument, the trend in the exposure times highly depends on the presence, amount and distribution of cloud cover in the atmosphere, as well as on the distribution of the absorbing gas. The presence of a global cloud layer at low altitudes ensures that a dominant fraction of any absorbing gas is present above the cloud layer, and it simply enhances the reflectivity of the disk. Thus, an atmosphere with a global cloud layer between 0.8 and 0.7 bar leads to the highest SNRs and the lowest exposure times required to make a robust detection. In contrast, the presence of a global cloud layer at high altitudes

makes it difficult to probe the atmosphere below resulting in low SNRs and higher exposure times. This difference is especially highlighted for observations of the H_2O 0.9–1 μm signal (see Table 3), where, depending on the instrument, it takes ~ 330 – 360 times longer to make an $SNR = 5$ detection for an atmosphere with a high-altitude global cloud layer. Depending on the absorbing gas, either an atmosphere with a global high altitude cloud layer or a clear atmosphere yield the lowest SNRs and the highest exposure times. Note that our O_2 exposure times for the clear sky scenario are higher than those

Table 4The Exposure Times Required to Make a Robust Detection ($\text{SNR} = 5$) of the H_2O 1.25–1.6 μm Absorption Band for the Six Types of Atmospheres Described Above

Type of Atmosphere	LUVOIR-A (hr)	LUVOIR-B (hr)	HWO (hr)	Habex-SS (hr)
Patchy clouds with high cloud abundance	0.44	7.75	74.83	18.85
Patchy clouds with mean cloud abundance	0.55	9.67	93.23	24.16 hr
Patchy clouds with low cloud abundance	0.71	12.29	118.36	31.34
Global cloud layer from 0.8–0.7 bar	0.15	2.58	24.94	6.1
Global cloud layer from 0.34–0.24 bar	5.29	81	757.95	647.04
No clouds	4.56	79.98	756.44	230.95

Note. Exo-Earth is placed 10 pc away at quadrature.**Table 5**The Exposure Times Required to Make a Robust Detection ($\text{SNR} = 5$) of the O_3 0.2–0.4 μm Band for the Six Types of Atmospheres

Type of Atmosphere	LUVOIR-A (hr)	LUVOIR-B (hr)	HWO (hr)	Habex-SS (hr)
Patchy clouds with high cloud abundance	0.23	0.9	2.57	1.22
Patchy clouds with mean cloud abundance	0.25	0.97	2.78	1.31
Patchy clouds with low cloud abundance	0.27	1.05	3.01	1.43
Global cloud layer from 0.8–0.7 bar	0.1	0.38	1.08	0.51
Global cloud layer from 0.34–0.24 bar	0.15	0.59	1.7	0.8
No clouds	0.41	1.61	4.61	2.17

computed in J. H. Checlair et al. (2021), as they assume simultaneous wavelength coverage and calculate the net SNR in all the three wavelength bands. In contrast, we only focus on the O_2 A line in the visible band. Similarly, the difference in the O_3 exposure times might be additionally caused by changes in the sampling algorithm of PSG (P. Saxena et al. 2021).

Since we expect an abundance of patchy clouds on exo-Earth atmospheres, the cloud-free case is a hypothetical scenario and not a baseline assumption. The three cases with varying levels of patchy cloud abundance are more realistic, and hence, a detailed comparison among them is necessary. The O_3 SNRs are not significantly affected by the amount of tropospheric patchy clouds, and hence show little variation. In contrast, the SNRs of O_2 and H_2O show a significant correlation with the amount of patchy clouds, as shown by the computed exposure times required to yield $\text{SNR} = 5$. Thus, depending on the atmospheric constituent, the amount of patchy clouds result in a 15%–60% variation in the exposure times for an HWO 6 m instrument. These variations would be confounded if the instrument does not have simultaneous wavelength coverage. For instance, HWO will take 143 hr to detect all three gases with $\text{SNR} = 5$ if the atmosphere has high cloud abundance versus 220 hr if the atmosphere has low cloud abundance, a 54% increase in exposure time. This has significant implications for observing programs dedicated to accurately characterizing exo-Earth atmospheres.

4. Discussion and Conclusions

To summarize, we construct an accurate 3D model of an exo-Earth using empirical 3D atmospheric data from the

MERRA-2 reanalysis package. We quantify the effects of clouds and cloud variability on the reflectance spectra and SNRs of key molecules by simulating observations of this exo-Earth with the GlobES module of PSG for atmospheres with different cloud distributions and abundances. Clouds enhance the continuum in the reflected light by increasing the albedo of the disk. Different amounts of cloud cover over the visible portions of the planet’s disk cause variations in the spectra of a rotating planet. These variations are more significant than the ones caused by the changing surface albedo of the visible disk. Figure 2 shows that the spectra of a cloudy planet show at max a $\sim 75\%$ variation in reflected flux at 0.5 μm for different rotational phases. In contrast, the cloud-free spectra only vary by $\sim 15\%$ at the same wavelength, due to the changing surface albedo. Depending on total cloud coverage and their vertical position, patchy clouds can increase or decrease the SNRs of all three atmospheric gases considered here, O_2 , H_2O , and O_3 , and thus enhance/diminish their detectability in exo-Earth atmospheres. The impact of cloud variability can potentially confound efforts to retrieve a stable baseline atmosphere for a planet—this is inherently because such a baseline is a physical approximation. Similar to transit studies of exoplanets, cloud variability and weather may have chromatic effects on planetary spectra (D. Powell et al. 2019) that may limit (T. J. Fauchez et al. 2019) or enhance the detection of key features depending on their magnitude relative to noise (E. M. May et al. 2021) and other factors. Importantly, observations of the Earth utilized in an “Earth as an Exoplanet” manner can play a key role in informing how such a variability may play these roles depending on different relevant temporal scales.

The impact of patchy clouds and weather variability for direct-imaging is relevant to the most proximate missions aimed at detecting and characterizing potential exo-Earths. The HWO's main goal is to identify and directly image at least 25 potentially habitable worlds—this target is based upon statistical yield calculations that require assumptions about both the astrophysical scene and planetary properties. Some of these planets are expected to have large fractions of water on the surface, and like the Earth, consequent abundant cloud cover. Cloud cover variability is likely to impact both detection and characterization of these worlds, thus influencing attainment of the required yield over a nominal mission design. Since cloud cover difference and the variability that may drive it are most apparent in between 0.3 and $0.7\ \mu\text{m}$ in the visible, this will likely have pronounced impacts on detection as recent work has found an optimum detection wavelength of $0.5\ \mu\text{m}$ for the majority of targets relevant to HWO (C. C. Stark et al. 2024). Similarly, the nonmonotonic relationships in SNR changes due to cloud variability and height for oxygen and water suggest that optimal wavelengths for the detection of some key biomarkers are also likely to be impacted in complicated ways by such a variability. Additional work exploring the general impact such a variability may have on the detection and characterization of a potential HWO sample of habitable planet candidates is important precursor work for an observation strategy. Critically, the mission plan may also require an understanding of the impact of weather variability on the observational budget required to meet key objectives. Given the 20%–50% variation in times to an $\text{SNR} = 5$ signal for key molecules in Tables 2–5, the budget required to achieve detection and characterization of a sufficient sample to achieve mission objectives should account for this uncertainty.

We note that precisely quantifying the effect of clouds on SNRs requires an understanding of the vertical distribution of clouds with respect to the vertical distribution of the atmospheric constituents. For example, O_2 and H_2O are abundant in the troposphere while O_3 is dominant much higher in the stratosphere. Thus, the differences in their SNR enhancements in the presence of clouds are a reflection of this distribution. We show that atmospheres with low-lying thick clouds produce the highest gaseous SNRs as such clouds greatly increase the albedo of the disk, and the low altitude of the cloud layer ensures that a majority of the atmospheric scale height is probed. On the other hand, high-altitude clouds make it difficult to probe the atmosphere below them and thus reduce the detectability of any gases abundant there. While observational constraints are unlikely to be obtained by HWO or other proximate planned direct-imaging missions, variability due to varying cloud coverage may be a novel way of constraining cloud altitude in some limited cases.

Using MERRA-2's historic record, we have shown that Earth shows significant variation in cloud abundance across different timescales. On average, Earth's total cloud abundance has increased over the past few decades. On an annual scale, Earth's cloud cover peaks in the northern summer months of June–August and subsequently decreases during the winter months. We expect any exo-Earth with some obliquity to show a seasonal pattern in cloud variability. This implies that the planet will have higher cloud abundance for a certain duration of its orbital period. Thus, there is an optimum period to observe such a planet if the goal is to detect atmospheric constituents and obtain sufficiently high gaseous SNRs within a

reasonable exposure time. However, to produce the highest observational yields, this optimum period should fortuitously coincide with the period when the planet is actually observable (within the bounds of the inner and outer working angle of the coronagraph and at an optimum orbital phase). Thus, an observation can underestimate the SNRs, especially if the planet has low seasonal cloud cover during the observation. This is further complicated by a possible degeneracy between the amount of cloud abundance and the concentration of gases while interpreting observed SNRs. In addition to seasonal cloud variation, terrestrial planets may also exhibit diurnal cloud variations due to rotation (given that they are sufficiently far away from their host star to escape tidal effects). If the planet is under observation for much longer than its rotational period, these diurnal variations will be averaged out. Taking multiple small exposures over an extended observation period might reveal periodic trends in planetary spectra and SNRs caused by the diurnal variation in cloud cover, and such trends can also be used to estimate the rotation period of the planet. There are however a number of caveats in leveraging cloud variability to optimize an observational strategy. First, we have only examined an initial general impact of water cloud coverage on the atmosphere—other factors such as variable hazes (such as those generated by volcanic eruptions) may also influence observations in transient ways. Variability signatures may or may not exceed noise levels for different systems, and the impact in both cases on retrieved parameters should be examined. Finally, variability due to sources external to the planet that are difficult to extricate from weather variability signatures such as time-varying signatures of exozodiacal dust (D. Defrère et al. 2012; A. Roberge et al. 2012; or the presence of additional bodies in the system, P. Saxena 2022) may also be degenerate and confounding factors. However, if the planets we target to directly image in the future are hoped to be Earth-like, we should expect cloud variability based upon our observations of the present-day Earth, and should consider and incorporate both the challenges and potential opportunity such a variability may provide.

Acknowledgments

We would like to thank Vincent Kofman, Geronimo Villanueva, and Allison Payne for conversations that helped improve the quality of this paper. The authors also acknowledge support from the Goddard Space Flight Center (GSFC) Sellers Exoplanet Environments Collaboration (SEEC), which is supported by the NASA Planetary Science Division's Research Program. This material is based upon work supported by NASA under award No. 80GSFC21M0002. The authors acknowledge the support and the resources provided by PARAM Brahma Facility under the National Supercomputing Mission, Government of India at the Indian Institute of Science Education and Research, Pune.

Appendix Configuration Files

The configuration files can be uploaded to the web interface or used with the API for PSG to simulate spectra, and are available on Zenodo: doi:10.5281/zenodo.14997824. There are four configuration files corresponding to the MERRA-2 data for four dates—2000 July 1 (randomly selected date for calibration), 1987 February 15 (low patchy cloud abundance),

2011 January 20 (closest to mean patchy cloud abundance), and 1999 July 7 (high patchy cloud abundance). Two additional files correspond to atmospheres with a low-altitude and a high-altitude global cloud layer.

ORCID iDs

Soumil Kelkar  <https://orcid.org/0009-0005-5118-4174>
 Ravi Kopparapu  <https://orcid.org/0000-0002-5893-2471>
 Joy Monteiro  <https://orcid.org/0000-0002-3932-3603>

References

- Arnold, L., Gillet, S., Lardière, O., Riaud, P., & Schneider, J. 2002, *A&A*, **392**, 231
- Brooke, T., Knacke, R., Encrenaz, T., et al. 1998, *Icar*, **136**, 1
- Buras, R., Dowling, T., & Emde, C. 2011, *JQSRT*, **112**, 2028
- Cahoy, K. L., Marley, M. S., & Fortney, J. J. 2010, *ApJ*, **724**, 189
- Checlair, J. H., Villanueva, G. L., Hayworth, B. P., et al. 2021, *AJ*, **161**, 150
- Defrère, D., Stark, C., Cahoy, K., & Beerer, I. 2012, *Proc. SPIE*, **8442**, 84420M
- Edwards, D. 1992, *GENLN2: A General Line-by-line Atmospheric Transmittance and Radiance Model. Version 3.0 Description and Users Guide* NCAR/TN-367+STR, Univ. Corporation for Atmospheric Research
- Faucher, T. J., Turbet, M., Villanueva, G. L., et al. 2019, *ApJ*, **887**, 194
- Friedl, M., & Sulla-Menashe, D. 2015, MCD12C1 MODIS/Terra+Aqua Land Cover Type Yearly L3 Global 0.05Deg CMG, NASA LP DAAC, doi:10.5067/MODIS/MCD12C1.006
- Gao, P., Wakeford, H. R., Moran, S. E., & Parmentier, V. 2021, *JGRE*, **126**, e06655
- Gaudi, B. S., Meyer, M., & Christiansen, J. 2021, The Demographics of Exoplanets, *ExoFrontiers: Big questions in exoplanetary science* (Bristol: IOP Publishing), **2**–1-2-21
- Gaudi, B. S., Seager, S., Mennesson, B., et al. 2020, The Habitable Exoplanet Observatory (HabEx) Mission Concept Study Final Report, arXiv:2001.06683
- Gelaro, R., McCarty, W., Suárez, M. J., et al. 2017, *JCLI*, **30**, 5419
- Global Modeling and Assimilation Office (GMAO) 2015a, MERRA-2 inst3_3d_asm_Nv: 3d,3-Hourly,Instantaneous, Model-Level, Assimilation, Assimilated Meteorological Fields V5.12.4, Greenbelt, MD, USA, Goddard Earth Sciences Data and Information Services Center (GES DISC), doi:10.5067/SUOQESM06LPK
- Global Modeling and Assimilation Office (GMAO) 2015b, MERRA-2 tavgM_3d_cld_Np: 3d,Monthly mean, Time-Averaged, Pressure-Level, Assimilation, Cloud Diagnostics V5.12.4, Greenbelt, MD, USA, Goddard Earth Sciences Data and Information Services Center (GES DISC), doi:10.5067/J9R0LXGH48JR
- Gordon, I. E., Rothman, L. S., Hargreaves, R., et al. 2022, *JQSRT*, **277**, 107949
- Grenfell, J. L., Stracke, B., von Paris, P., et al. 2007, *P&SS*, **55**, 661
- Gu, L., Fan, S., Li, J., et al. 2021, *AJ*, **161**, 122
- Hamdani, S., Arnold, L., Foellmi, C., et al. 2006, *A&A*, **460**, 617
- Hansen, J. E., & Hovenier, J. 1974, *JatS*, **31**, 1137
- Hearty, T., Song, I., Kim, S., & Tinetti, G. 2009, *ApJ*, **693**, 1763
- Helling, C. 2019, *AREPS*, **47**, 583
- Kaltenegger, L., Traub, W. A., & Jucks, K. W. 2007, *ApJ*, **658**, 598
- Kasting, J. F., Whitmire, D. P., & Reynolds, R. T. 1993, *Icar*, **101**, 108
- Kawashima, Y., & Rugheimer, S. 2019, *AJ*, **157**, 213
- Keller-Rudek, H., Moortgat, G. K., Sander, R., & Sörensen, R. 2013, *ESSD*, **5**, 365
- King, M. D., Platnick, S., Menzel, W. P., Ackerman, S. A., & Hubanks, P. A. 2013, *ITGRS*, **51**, 3826
- Kitzmann, D., Patzer, A., von Paris, P., et al. 2010, *A&A*, **511**, A66
- Kitzmann, D., Patzer, A. B. C., von Paris, P., Godolt, M., & Rauer, H. 2011a, *A&A*, **534**, A63
- Kitzmann, D., Patzer, A. B. C., von Paris, P., Godolt, M., & Rauer, H. 2011b, *A&A*, **531**, A62
- Kofman, V., Villanueva, G. L., Faucher, T. J., et al. 2024, The Pale Blue Dot: Using the Planetary Spectrum Generator to Simulate Signals from Hyperrealistic Exo-Earths, *PSJ*, **5**, 197
- Kokaly, R., Clark, R., Swayze, G., et al. 2017, USGS Spectral Library Version 7: U.S. Geological Survey Data Series 1035, 61 p., doi:10.3133/ds1035
- Kopparapu, R., Arney, G., Haqq-Misra, J., Lustig-Yaeger, J., & Villanueva, G. 2021, *ApJ*, **908**, 164
- Kreidberg, L., Bean, J. L., Désert, J.-M., et al. 2014, *Natur*, **505**, 69
- Line, M. R., Knutson, H., Deming, D., Wilkins, A., & Desert, J.-M. 2013, *ApJ*, **778**, 183
- Loeb, N. G., Doelling, D. R., Wang, H., et al. 2018, *JCLI*, **31**, 895
- LUVOR Team 2019, arXiv:1912.06219
- Marley, M. S., Ackerman, A. S., Cuzzi, J. N., & Kitzmann, D. 2013, Clouds and Hazes in Exoplanet Atmospheres, *Comparative Climatology of Terrestrial Planets* (Tucson, AZ: Univ. Arizona Press), 367
- Marley, M. S., Gelino, C., Stephens, D., Lunine, J. I., & Freedman, R. 1999, *ApJ*, **513**, 879
- May, E. M., Taylor, J., Komacek, T. D., Line, M. R., & Parmentier, V. 2021, *ApJL*, **911**, L30
- Montanes-Rodriguez, P., Pallé, E., Goode, P., & Martín-Torres, F. 2006, *ApJ*, **651**, 544
- Montmessin, F., Gondet, B., Bibring, J.-P., et al. 2007, *JGRE*, **112**, E11590
- National Academies of Sciences, Engineering, and Medicine 2023, Pathways to Discovery in Astronomy and Astrophysics for the 2020s (Washington, DC: The National Academies Press)
- Powell, D., Loudon, T., Kreidberg, L., et al. 2019, *ApJ*, **887**, 170
- Roberge, A., Chen, C. H., Millan-Gabet, R., et al. 2012, *PASP*, **124**, 799
- Rossow, W. B., & Lacis, A. A. 1990, *JCLI*, **3**, 1204
- Rothman, L. S., Gordon, I., Barber, R., et al. 2010, *JQSRT*, **111**, 2139
- Sánchez-Lavega, A., Pérez-Hoyos, S., & Hueso, R. 2004, *AmJPh*, **72**, 767
- Saxena, P. 2022, *ApJL*, **934**, L32
- Saxena, P., Villanueva, G. L., Zimmerman, N. T., Mandell, A. M., & Smith, A. J. R. W. 2021, *AJ*, **162**, 30
- Segura, A., Kasting, J. F., Meadows, V., et al. 2005, *AsBio*, **5**, 706
- Segura, A., Krelove, K., Kasting, J. F., et al. 2003, *AsBio*, **3**, 689
- Sing, D. K., Wakeford, H. R., Showman, A. P., et al. 2015, *MNRAS*, **446**, 2428
- Snee, M., & Ubachs, W. 2005, *JQSRT*, **92**, 293
- Stamnes, K., Tsay, S.-C., Wiscombe, W., & Jayaweera, K. 1988, *ApOpt*, **27**, 2502
- Stamnes, K., Tsay, S.-C., Wiscombe, W., & Laszlo, I. 2000, DISORT, a General-Purpose Fortran Program for Discrete-Ordinate-Method Radiative Transfer in Scattering and Emitting Layered Media: Documentation of Methodology (No. DISORT Report v1.1), <https://www.libradtran.org/lib/exe/fetch.php?media=disortreport1.1.pdf>
- Stark, C. C., Latouf, N., Mandell, A. M., & Young, A. 2024, *JATIS*, **10**, 014005
- Stowe, L., McClain, E., Carey, R., et al. 1991, *AdSpR*, **11**, 51
- Sudarsky, D., Burrows, A., & Hubeny, I. 2003, *ApJ*, **588**, 1121
- Tinetti, G., Rashby, S., & Yung, Y. 2006, *ApJ*, **644**, L129
- Vasquez, M., Schreier, F., García, S. G., et al. 2013, *A&A*, **557**, A46
- Villanueva, G., Mumma, M., Novak, R., et al. 2015, *Sci*, **348**, 218
- Villanueva, G. L., Liuzzi, G., Faggi, S., et al. 2022, Fundamentals of the Planetary Spectrum Generator (Washington, DC: NASA Goddard Space Flight Center)
- Villanueva, G. L., Smith, M. D., Protopapa, S., Faggi, S., & Mandell, A. M. 2018, *JQSRT*, **217**, 86
- Wang, J., Mawet, D., Ruane, G., et al. 2017, *Proc. SPIE*, **10400**, 104000Z
- Wolff, M., Smith, M., Clancy, R., et al. 2009, *JGRE*, **114**, E00D04
- Wu, D., Hu, Y., McCormick, M. P., & Yan, F. 2011, *IJRS*, **32**, 1269
- Wylie, D., Jackson, D. L., Menzel, W. P., & Bates, J. J. 2005, *JCLI*, **18**, 3021
- Young, A. H., Knapp, K. R., Inamdar, A., Hankins, W., & Rossow, W. B. 2018, *ESSD*, **10**, 583